


---

This is the **accepted version** of the journal article:

Creus, Jordi; Drouet, Samuel; Suriñach, Santiago; [et al.]. «Ligand-Capped Ru Nanoparticles as Efficient Electrocatalyst for the Hydrogen Evolution Reaction». ACS Catalysis, Vol. 8, Issue 12 (December 2018), p. 11094-11102. DOI 10.1021/acscatal.8b03053

---

This version is available at <https://ddd.uab.cat/record/289779>

under the terms of the  <sup>IN</sup> COPYRIGHT license

# Ligand-Capped Ru Nanoparticles as Efficient Electrocatalyst for the Hydrogen Evolution Reaction

Jordi Creus<sup>a,b</sup>, Samuel Drouet<sup>b</sup>, Santiago Suriñach<sup>c</sup>, Pierre Lecante<sup>d</sup>, Vincent Collière<sup>b</sup>, Romuald Poteau<sup>e</sup>, Karine Philippot<sup>b,\*</sup>, Jordi García-Antón<sup>a,\*</sup>, Xavier Sala<sup>a,\*</sup>

<sup>a</sup> Departament de Química, Universitat Autònoma de Barcelona, Cerdanyola del Vallès, 08193 Barcelona, Spain; <sup>b</sup> LCC-CNRS, Université de Toulouse, CNRS, UPS, 205 Route de Narbonne, BP44099, 31077 Toulouse Cedex 4, France; <sup>c</sup> Departament de Física, Universitat Autònoma de Barcelona, Cerdanyola del Vallès, 08193 Barcelona, Spain; <sup>d</sup> CNRS, CEMES (Centre d'Elaboration de Matériaux et d'Etudes Structurales), 29 rue J. Marvig, F-31055 Toulouse, France; <sup>e</sup> LPCNO, Université de Toulouse, CNRS, INSA, UPS, 135 avenue de Rangueil, F-31077 Toulouse Cedex 4, France.

**KEYWORDS:** Ruthenium, Nanoparticles, Water Splitting, Electrocatalysis, Hydrogen Evolution Reaction, Energy

---

**ABSTRACT** Multielectron reductions such as the hydrogen evolution reaction (HER) play an important role in the development of nowadays energy economy. Herein, the application of the organometallic approach as synthetic method allows obtaining very small, ligand-capped but also highly active ruthenium nanoparticles (RuNPs) for the HER in both acidic and basic media. When deposited onto glassy carbon, the catalytic activity of this nanomaterial in 1 M H<sub>2</sub>SO<sub>4</sub> solution is highly dependent on the oxidation state of the NPs surface, being metallic Ru sites clearly more active than RuO<sub>2</sub> ones. In sharp contrast, in 1 M NaOH as electrolyte, the original Ru/RuO<sub>2</sub> mixture is maintained even under reductive conditions. Estimation of surface active sites and electroactive surface area (ECSA) allowed benchmarking this catalytic system, confirming its leading performance among HER electrocatalysts reported at both acidic and basic pH. Thus, in 1 M NaOH condition it displays lower overpotentials ( $\eta_0 \approx 0$  mV,  $\eta_{10} = 25$  mV) than those of commercial Pt/C and Ruthenium black (Rub), and also fairly outperforms them in short and long-term stability tests. In 1 M H<sub>2</sub>SO<sub>4</sub> solution, it clearly outdoes commercial Rub and is competitive or even superior to commercial Pt/C, working at very low overpotentials ( $\eta_0 \approx 0$  mV,  $\eta_{10} = 20$  mV) with a Tafel slope of 29 mV·dec<sup>-1</sup>, achieving TOFs as high as 17 s<sup>-1</sup> at  $\eta = 100$  mV and reaching a current density of  $|j| = 10$  mA·cm<sup>-2</sup> for at least 12h without any sign of deactivation.

**KEYWORDS:** Ruthenium, Nanoparticles, Water Splitting, Electrocatalysis, Hydrogen Evolution Reaction, Energy

---

## INTRODUCTION

The depletion of fossil fuels due to the increasing energy demand and the high levels of greenhouse gases directly related to climate change make the development of less polluting and renewable energy sources a central challenge for the scientific community. In this context, the use of sunlight to assist water splitting following the principle of artificial photosynthesis is a very attractive solution.<sup>1</sup> However, water splitting needs efficient catalysts for the half cell reactions involved, namely releasing electrons and protons from the oxidation of water (oxygen evolution reaction; OER) and their subsequent use to reduce protons into H<sub>2</sub> (hydrogen evolution reaction; HER). In the particular case of HER, despite Pt-based catalysts show the highest efficiencies in acidic media with minimum overpotentials and fast kinetics, their cost and stability issues at other pH values boost research on potential

substitutes both at molecular<sup>2</sup> and colloidal/heterogeneous level.<sup>3</sup>

Nanostructured catalysts, as illustrated by numerous results from heterogeneous (supported species) or colloidal catalysis, present several attractive properties compared to molecular complexes.<sup>4</sup> Thus, nanomaterial-based electrocatalysts are expected to display higher performance thanks to their high density of active sites (typically low for electrodes with grafted molecular catalysts) but also an enhanced stability.<sup>5</sup> This is already proven for numerous catalytic reactions<sup>6,7</sup> and more recently for water-splitting.<sup>8</sup> For the HER, metals such as Ni, Co, Mo or Pt have been studied as nanostructured catalysts with interesting activities (see Tables S1 and S2 in the SI). Curiously, Ru nanomaterials did not show impressive activity in this reaction<sup>9-12</sup> up to the last two years, when a few cathodes prepared with Ru-nanosized species appeared as potential substitutes to Pt-based electrodes (see Tables

S1 and S2 in the SI).<sup>13-20</sup> As the prohibitive price and scarcity of platinum make it unsuitable for large-scale commercial applications, these contributions open the way for novel developments of Ru-based electro-catalysts. This would constitute an alternative to reduce the cost of the catalyst, the price of Ru being 1/4 that of Pt. The best performing Ru systems are prepared through complex synthetic protocols such as the condensation of organic precursors that direct the nucleation/growth of the Ru nanoparticles (NPs) and subsequent annealing to generate a conductive carbon matrix from the organic part,<sup>16,17</sup> or the direct assembly of a metal precursor (RuCl<sub>3</sub>) in a hierarchically-ordered carbon-based electrode followed by an annealing step.<sup>20</sup> These cathodes are thus composite materials made of RuNPs embedded into carbon matrices that strongly affect their catalytic behavior and do not permit to finely tune the active sites. Moreover, it is noteworthy that most of the reported nanocatalysts for HER suffer of lack of well-defined structures, disabling a proper correlation between the characteristics of the nanospecies and their catalytic properties while it is a key-point to optimize a catalytic reaction. In consequence, the design of finely controlled metal NPs should offer interesting perspectives to better understand the crucial parameters to develop nanostructured catalysts with increased performances, both in terms of efficiency and stability. For this purpose, the organometallic approach proved to be an efficient method, allowing to get very small NPs with a narrow size-distribution and controllable surface properties while using mild reaction conditions for their preparation.<sup>21,22</sup> This has been particularly demonstrated for RuNPs,<sup>23-25</sup> but also for other metals,<sup>26</sup> with remarkable properties in catalysis. Given the recent literature data on Ru nanostructured catalysts for HER, we decided to design and evaluate some Ru nanomaterials for this catalysis, applying the principles of the organometallic synthesis. We published very recently on a porous Ru nanomaterial prepared by this method that gave rise to high electrocatalytic performance and excellent durability for HER.<sup>19</sup> This material made of RuNPs of ca. 21 nm in size exhibited an overpotential of 83 mV at a current density of 10 mA·cm<sup>-2</sup> and an excellent durability up to 12h in 0.5 M H<sub>2</sub>SO<sub>4</sub>.

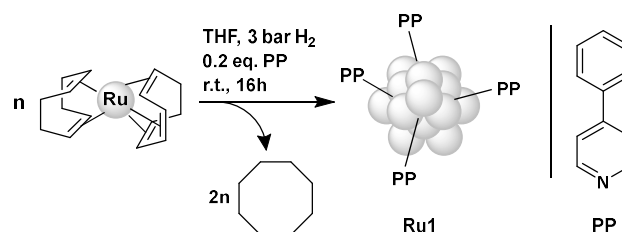
Herein, we report on the design of a novel nanostructured Ru catalyst constituted of 1.5 nm RuNPs capped with the 4-phenylpyridine ligand and its evaluation in the HER. This nanomaterial shows very low overpotentials ( $\eta$ ), fast kinetics and excellent durability in both acidic and basic electrolytes, clearly outperforming commercial Ru black and being competitive to commercial Pt/C under the same reaction conditions. The catalytic performance of this new cathode is benchmarked with the state-of-the-art HER electrocatalysts and the factors controlling its activity are unraveled by combining spectroscopic, electrochemical and computational techniques.

## RESULTS AND DISCUSSION

### Synthesis and characterization of RuNPs.

The Ru nanomaterial object of this study has been easily synthesized following the organometallic approach (Scheme 1), namely by decomposing the [Ru(cod)(cot)] (cod = 1,5-cyclooctadiene; cot = 1,3,5-cyclooctatriene)

complex under H<sub>2</sub> atmosphere (3 bar) and at room temperature (r.t.), using THF as a solvent and 4-phenylpyridine (PP) as a stabilizing ligand ([PP]/[Ru]= 0.2 molar equivalent). The advantages of the precursor used here are the fast decomposition under H<sub>2</sub> which leads to the formation of very small RuNPs as well as the release of cyclooctane as only by-product which is facile to eliminate under vacuum. By this way, only the ligand voluntarily added as stabilizing agent (here the 4-phenylpyridine) is present on the metal surface, in addition to some THF and hydrides. Following this procedure, a black colloidal dispersion was obtained from which the RuNPs (sample **Ru1**) were isolated under the form of a black powder after precipitation by addition of pentane and drying under vacuum. Complementary techniques were applied to characterize the obtained nanomaterial.



**Scheme 1.** Synthesis of **Ru1** with PP ligand chemical structure.

Transmission electron microscopy (TEM) analysis carried out from the crude colloidal solution after deposition of a drop on a carbon-covered copper grid revealed the presence of very small NPs (Figure 1). They appear well-dispersed on the TEM grid (Figure 1a) with only a few agglomerates noticed, and display an average diameter of  $1.5 \pm 0.3$  nm (by considering the smallest dimension) with a narrow size distribution (Figure 1c) thus indicating a good control in size. At higher magnification (Figure 1b), some NPs close to each other or even coalesced are observed and crystalline plans are visible.

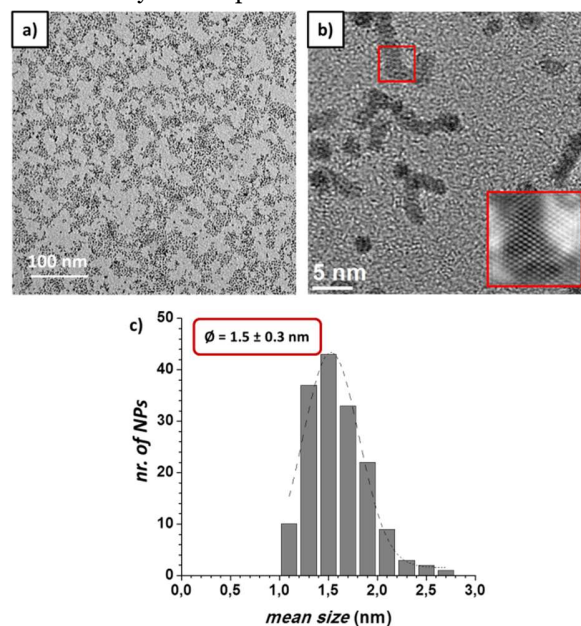


**Figure 1.** TEM images of **Ru1** at low (a) and high (b) magnification and size histogram (c) established from image (a).

HRTEM images and electron diffraction patterns on a purified sample confirmed its crystalline character and allowed to measure interplanar distances (Figure S1) namely 0.21, 0.16, 0.13 and 0.11 nm, values in agreement with those of the (101), (102), (110) and (112) planes of the hexagonal compact crystalline (hcp) structure of bulk ruthenium. EDX analysis showed the absence of oxygen thus evidencing the presence of Ru metal particles (Figure S2 and S3). Wide-angle X-Ray scattering (WAXS) analysis also confirmed the metallic character of the RuNPs and their hcp structure (Figure S4). A coherence length of ca. 2.3 nm could be determined, significantly larger than the average size from TEM. Coherence length is a direct measurement of the maximum size of crystalline domains, and in case of size dispersion, the weight of larger NPs is quite high. Moreover, the monotonous decrease profile of the distribution of distances (Figure S4-bottom) is consistent with smaller sizes. These results indicate a limited coalescence of small metallic NPs in the sample. It is however delicate to accurately evaluate the coalescence ratio of NPs without assumptions on their final shape.

Elemental (EA; Table S3) and thermogravimetric (TGA; Figure S5) analyses of **Ru1** led in both cases to an organic content in the sample of ca. 15% and therefore a high Ru content of ca. 85%. This Ru nanomaterial burned spontaneously when exposed to the air in solid state. Such a behavior was previously observed with other RuNPs of similar sizes and stabilized with different ligands.<sup>23</sup> This phenomenon reveals a high reactive metal surface assumed to derive from the small size of the NPs and the accessibility of their surface although being coated by the PP ligand. Surface hydride quantification was performed by norbornene hydrogenation in a methodology previously reported in our group, obtaining a 1.1 H/Ru<sub>surf</sub> ratio (Ru<sub>surf</sub> are surface ruthenium atoms), a value that is similar to those obtained with other systems of polymer- and ligand-stabilized RuNPs such as 1.3 for Ru-PVP (PVP: *N*-polyvinylpyrrolidone) and Ru-HDA (HDA: hexadecylamine) NPs or 1.1 for Ru-dppd (dppd: 1,10-bis(diphenylphosphino)decane) nanoparticles.<sup>23,27</sup>

Density Functional Theory (DFT) calculations performed on a bare 1nm model and on its 1.2H/Ru<sub>surf</sub> hydrogenated counterpart<sup>28</sup> attested that the coordination of the PP ligand at the ruthenium surface can occur through two coordination modes. There is a competition between a vertical adsorption mode, ruled out by the  $\sigma$ -donation of the nitrogen lone pair (see Figure 2a,  $1\sigma_{\text{tip}}$  mode) and an aromatic  $\pi$ -to-metal surface interaction, with a flat-lying configuration of PP where each aromatic cycle exhibits the well-known  $\mu_3:\eta^2:\eta^2:\eta^2$  face-capping mode of benzene (see Figure 2a,  $1\pi_{\text{001}}$  mode).<sup>29</sup> The  $\pi$  coordination of a single PP on one (001) facet of the bare RuNP model is stable by -83.2 kcal.mol<sup>-1</sup>, whereas the  $\sigma$  bond is weaker by 49.8 kcal.mol<sup>-1</sup> (-33.4 kcal.mol<sup>-1</sup> see Table S4). The adsorption strength of PP on an edge was also evaluated, with an  $\eta^6$ -benzene ring and a  $\mu:\eta^3:\eta^3$ -pyridine (see Figure 2a,  $1\pi_{\text{edge}}$  mode) showing a stability by -63.6 kcal.mol<sup>-1</sup> (see table S4). For comparison, in an hydrogenated Ru<sub>55</sub> model with 1.2H per surface Ru atom (Ru<sub>55</sub>H<sub>53</sub>),<sup>28</sup> whereas the  $\sigma$

adsorption strength is very little affected by the presence of surface H atoms ( $1\sigma_{\text{tip}}$ : -32.1 kcal.mol<sup>-1</sup> on Ru<sub>55</sub>H<sub>53</sub> vs -33.4 kcal.mol<sup>-1</sup> on the naked RuNP), the  $\pi$  interaction becomes significantly less competitive ( $1\pi_{\text{001}}$ : -48.8 kcal.mol<sup>-1</sup> vs. -83.2 kcal.mol<sup>-1</sup>). In contraposition, the adsorption strength of PP on an edge,  $1\pi_{\text{edge}}$ , involves a weaker segregation of the surface H atoms than the  $1\pi_{\text{001}}$  mode does, with an adsorption energy similar to the bare NP case ( $1\pi_{\text{edge}}$ : -59.0 kcal.mol<sup>-1</sup> vs. -63.6 kcal.mol<sup>-1</sup>), making again a  $\pi$  coordination mode significantly more stable than the  $\sigma$  grafting.

Another interesting point is the evaluation of the optimal number of PP ligands that the Ru<sub>55</sub>H<sub>53</sub> model can accommodate. What is obvious from Figure 2b is that from a geometrical point of view it is possible to graft more  $\sigma$ -coordinated PPs than  $\pi$ -coordinated PPs within a unit surface area. Our modelling results (see discussion in the SI) suggest that (i) the saturation is reached around 11 PPs on this model (*i.e.* 0.27 PP/Ru<sub>surf</sub> with this fixed 1.20 H/Ru<sub>surf</sub> composition, see Figure 2), with the co-adsorption of 9  $\sigma$ -PPs and 2  $\pi$ -PPs (see Figure 2b) being more stable than the adsorption of 12  $\sigma$ -PPs (-265.2 kcal.mol<sup>-1</sup> vs. -243.4 kcal.mol<sup>-1</sup>); (ii) the two  $\sigma$  and  $\pi$  grafting modes are expected to both occur on a given RuNP, with a versatile and rather strong  $\pi$  coordination.

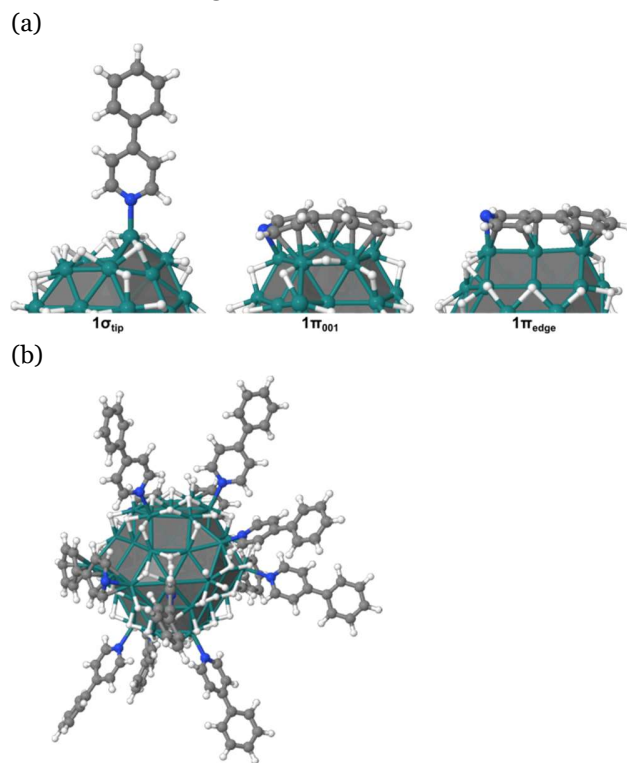


**Figure 2.** (a)  $\sigma$  and  $\pi$  coordination modes of PP on the Ru<sub>55</sub>H<sub>53</sub> model (the faceting of the metal surface is highlighted. Geometries of PP and of the grafting metal site on the bare Ru<sub>55</sub> model are very similar). (b) PP-protected 1 nm RuNP (Ru<sub>55</sub>H<sub>53</sub>σPP<sub>9</sub>πPP<sub>2</sub>).

Given the high reactivity of **Ru1** nanomaterial observed when exposed to air, a protection appeared necessary to preserve its morphology before the electrocatalytic studies. For this purpose, **Ru1** was treated in the solid state by



slow oxygen diffusion at r.t., leading to the **Ru2** nano-material (Scheme 2). The effect of this treatment on the oxidation state of the RuNPs was characterized by HRTEM-EDX (Figures S6-S7), WAXS (Figure S8) and X-Ray photoelectron spectroscopy (XPS, Figure S9). The three techniques indicated the presence of a mixture of Ru metal and Ru oxide in **Ru2**. This evidences a partial oxidation of the particles that probably took place only at their surface, passivating them and avoiding an irreversible degradation. TGA and EA data for **Ru1** and **Ru2** (Figure S5 and Table S3) show similar % of organic content in both samples, as well as an invariable PP/Ru ratio, thus confirming the presence of the PP ligand also after passivation.

**Electrocatalytic studies in HER.** The HER catalytic performance of **Ru2** was evaluated in both acidic and basic media (1 M H<sub>2</sub>SO<sub>4</sub> and 1 M NaOH, respectively). For comparison purposes, the performances of commercial Pt/C and Ru black (Rub) were tested under the same experimental conditions. A THF dispersion of **Ru2** was drop-casted onto a glassy carbon rotating disk electrode (RDE/GC) (see the Materials and Methods section and Scheme S1 for further details on electrode preparation), to generate the **Ru2-GC** working electrode, which was introduced in a three-electrode cell together with a Saturated Calomel Electrode (SCE, KCl sat.) and a Pt grid as reference and counter electrodes, respectively. Working electrodes based on Pt/C and Rub were prepared using the same protocol and metal loading. The representative hydrogen evolution linear sweep voltammetry (LSV) polarization curves of the three systems at a scan rate of 10 mV·s<sup>-1</sup> and 3000 rpm are given in the left part of Figure 3 (a, 1 M H<sub>2</sub>SO<sub>4</sub>; b, 1 M NaOH). In 1 M aqueous H<sub>2</sub>SO<sub>4</sub> solution, both **Ru2-GC** and Pt/C show very small onset overpotential ( $\eta_0$ ) close to 0 mV, much lower than that of Rub (70 mV). Together with  $\eta_0$ , another benchmarking parameter to compare the performance of heterogeneous catalysts is the overpotential value needed to achieve a current density of  $|j| = 10 \text{ mA}\cdot\text{cm}^{-2}$  ( $\eta_{10}$ ) that corresponds to the approximate current density expected for a 10% efficient solar-to-fuel conversion photoelectrochemical cell under 1 Sun illumination.<sup>30,31</sup> **Ru2-GC** reaches this current density at  $\eta_{10} = 35 \text{ mV}$  against 27 mV and 150 mV for Pt/C and Rub, respectively. The obtained  $\eta_0$  and  $\eta_{10}$  values situate **Ru2-GC** within the best Ru-based systems reported so far (See Table S1 for a comparison between the state-of-the-art HER electrocatalysts in acidic electrolytes), and also very close to Pt/C.

The catalytic performance of the system in 1 M aqueous H<sub>2</sub>SO<sub>4</sub> solution can be significantly improved when submitted to a current-controlled bulk electrolysis at  $j = -10 \text{ mA}\cdot\text{cm}^{-2}$  for 20 min. As presented in Figure 3a, the resulting reduced system (**Ru1-GC**) shows a  $\eta_{10}$  of 20 mV, that is 7 and 130 mV lower than Pt/C (27 mV) and Rub (150 mV), respectively, and reaches current densities as high as 1 A·cm<sup>-2</sup> at an overpotential of only 120 mV.

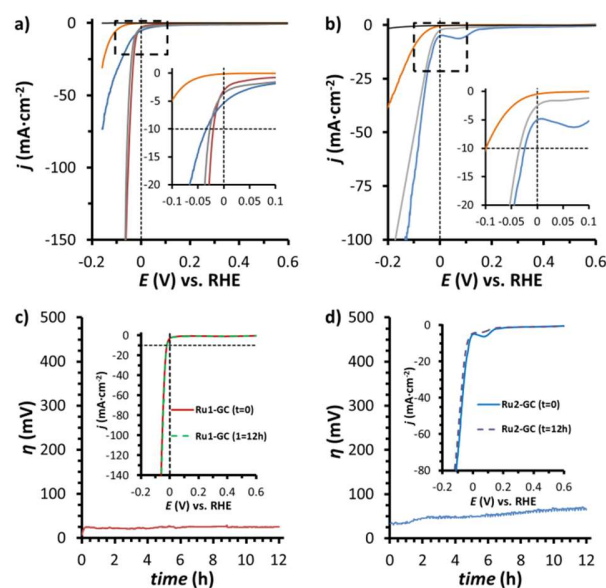


**Figure 3.** a) Polarization curves of **Ru1-GC** (red), **Ru2-GC** (blue), Rub (orange), commercial Pt/C (grey) and bare RDE (black) in a 1 M H<sub>2</sub>SO<sub>4</sub> solution at a 10 mV·s<sup>-1</sup> scan rate and inset of the onset overpotential zone. b) Polarization curves of **Ru2-GC** (blue), Rub (orange), commercial Pt/C (grey) and bare RDE (black) in a 1 M NaOH solution at a 10 mV·s<sup>-1</sup> scan rate and inset of the onset overpotential zone. c) 12-hour bulk electrolysis experiment of **Ru1-GC** at  $j = -10 \text{ mA}\cdot\text{cm}^{-2}$  in 1 M H<sub>2</sub>SO<sub>4</sub> solution; inset, LSV experiment before and after bulk electrolysis. d) 12-hour bulk electrolysis experiment of **Ru2-GC** at  $j = -10 \text{ mA}\cdot\text{cm}^{-2}$  in 1 M NaOH solution; inset, LSV experiment before and after bulk electrolysis.

In order to shed light on the nature of the new species formed in 1 M H<sub>2</sub>SO<sub>4</sub> under reductive conditions, both **Ru1-GC** and **Ru2-GC** were analyzed by XPS (Figure 4). As already mentioned for **Ru2**, a mixture of metallic Ru and RuO<sub>2</sub> is observed for the **Ru2-GC** electrode with Ru 3d<sub>5/2</sub> peaks centered at 279.8 eV (metallic Ru) and 280.8 eV (RuO<sub>2</sub>).<sup>32</sup> For the **Ru1-GC** electrode, a total disappearance of the Ru 3d<sub>5/2</sub> peak at 280.8 eV is noticed, thus indicating the reduction of superficial Ru(IV) to metallic Ru under catalytic conditions. After the reductive treatment some **Ru1** material was recovered from the electrode surface in order to analyze the presence/absence of PP ligand after the applied reductive potential. TGA analysis (Figure S10) showed similar organic content than its partially oxidized counterpart (compare Figures S5 and S10), thus confirming the presence of the PP ligand in the nano-material after reductive treatment. As shown in Figure S11a, the passivation process of **Ru1-GC** can be monitored electrochemically by dipping this electrode in an aerated 1 M H<sub>2</sub>SO<sub>4</sub> solution and recording LSV polarization curves at different times. As surface metallic Ru in **Ru1-GC** gets oxidized and RuO<sub>2</sub> is formed (see XPS data in Figure 4a) a progressive decrease of the catalytic current associated to the HER is observed, with LSV-4h (Figure S11a) finally resembling the electrochemical signature of **Ru2-GC**.

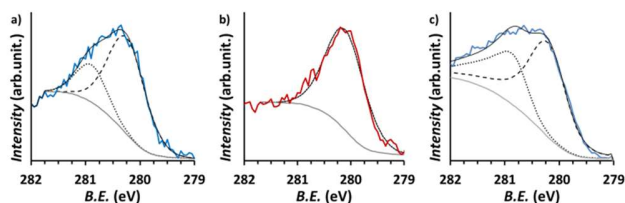


**Figure 4.** XPS analysis of a) **Ru2-GC** (blue), b) **Ru1-GC** (red) after 20 minutes bulk electrolysis at  $j = -10 \text{ mA}\cdot\text{cm}^{-2}$  in 1 M  $\text{H}_2\text{SO}_4$ , and c) **Ru2-GC** (blue) after 20 minutes bulk electrolysis at  $j = -10 \text{ mA}\cdot\text{cm}^{-2}$  in 1 M NaOH. Background (grey), metallic-Ru component (Ru  $3d_{5/2}$ -279.8, dashed black),  $\text{RuO}_2$ -component (Ru  $3d_{5/2}$ -280.8, dotted-black), envelope (bold).

The different nature and catalytic performance of **Ru1-GC** and **Ru2-GC** in 1 M  $\text{H}_2\text{SO}_4$  are evidenced through their corresponding Tafel plots (see Figure 5a). **Ru1-GC** shows a very low Tafel slope ( $29 \text{ mV}\cdot\text{dec}^{-1}$ ), inferior to that of Pt/C ( $32 \text{ mV}\cdot\text{dec}^{-1}$ ) and Rub ( $65 \text{ mV}\cdot\text{dec}^{-1}$ ) under the same reaction conditions and metal loading, thus pointing to a Tafel-Volmer mechanism where the rate-determining step is the formation and desorption of molecular  $\text{H}_2$  at the catalyst surface, by the recombination of two metal-hydride species.<sup>33</sup> Thus, **Ru1-GC** is able to reach high current densities at low overpotentials, a critical characteristic in order to attain practical applications. Contrarily, the  $106 \text{ mV}$  Tafel slope observed for **Ru2-GC** indicates a Tafel-Heyrovsky mechanism and the need of working at high overpotentials in order to reach relevant HER current densities.

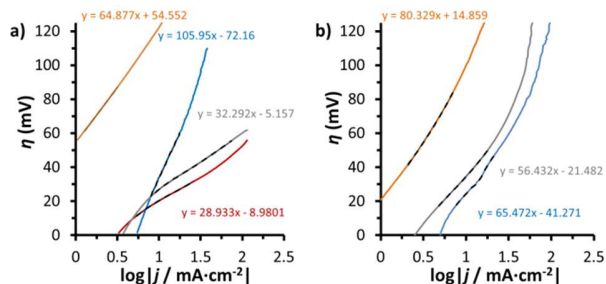


**Figure 5.** Tafel plot of **Ru1-GC** (red), **Ru2-GC** (blue), commercial Rub (orange) and commercial Pt/C (grey) a) in 1 M  $\text{H}_2\text{SO}_4$  and b) 1 M NaOH.

The HER performance of **Ru2-GC** in 1 M NaOH is also remarkable, with  $\eta_0$  of ca.  $0 \text{ mV}$  and  $\eta_{10}$  of  $25 \text{ mV}$ , values lower than those of Pt/C ( $5$  and  $35 \text{ mV}$ , respectively) and Rub ( $50$  and  $125 \text{ mV}$ , respectively), under the same reaction conditions. These values situate **Ru2-GC** within the best Ru-based systems reported so far in basic media (See Table S2 for a comparison between the state-of-the-art HER catalysts in basic electrolytes). In contrast to its behavior in 1 M  $\text{H}_2\text{SO}_4$ , **Ru2-GC** does not evolve under reductive conditions (current-controlled bulk electrolysis at  $j = -10 \text{ mA}\cdot\text{cm}^{-2}$  for 20 minutes) in 1 M NaOH, showing identical electroactivity before and after the reductive treatment (Figure S11b). Additionally, freshly prepared **Ru1-GC** oxidizes much faster in basic (Figure S11b) than in acidic media (Figures S11a). These results confirm, as expected, the higher stability of the  $\text{RuO}_2$  phase under basic conditions that is further corroborated by XPS analysis of the electrolyzed sample (Figure 4c). Comparison of

Figures 4a and 4c evidences a similar nature for both species, and the stability of the  $\text{RuO}_2$  phase present at the surface of **Ru2-GC** under reductive basic conditions. Analysis of the Tafel plot in 1 M NaOH solution (Figure 5b) shows a slope of  $65 \text{ mV}\cdot\text{dec}^{-1}$  for **Ru2-GC**,  $80 \text{ mV}\cdot\text{dec}^{-1}$  for Rub and  $56 \text{ mV}\cdot\text{dec}^{-1}$  for Pt/C.

The electrocatalytic performance and short-term stability of **Ru1-GC** (1 M  $\text{H}_2\text{SO}_4$ ) and **Ru2-GC** (1 M NaOH) was further compared with that of other electrocatalysts following the benchmarking methodology reported by Jaramillo *et al.*<sup>34</sup> From the capacitive current in a non-Faradaic region, which is only associated with double-layer charging, the double-layer capacitance ( $C_{\text{DL}}$ ) was estimated. Then, the electrochemically active surface area (ECSA) of both electrodes was calculated from the obtained  $C_{\text{DL}}$  (Figures S13-S14). The roughness factor (RF) was calculated by dividing the estimated ECSA by the geometric area of the electrode. The ECSA value allows calculating the specific current density ( $j_s$ ) of the electrode (current density per “real” electroactive area of the system) at a given overpotential. The obtained values of  $\eta_{10}$  at time  $t=0$  and  $t=2\text{h}$  and  $j_s$  at  $\eta = 100 \text{ mV}$  ( $j_{s(\eta=100)}$ ) are reported in Tables S5-S6 and plotted in Figure S15 together with those reported for selected HER catalysts benchmarked with the same methodology in acidic 1 M  $\text{H}_2\text{SO}_4$  and basic 1 M NaOH solutions. Only systems with  $\eta_{10} < 100 \text{ mV}$  (in 1 M  $\text{H}_2\text{SO}_4$ ) and  $\eta_{10} < 150 \text{ mV}$  (in 1 M NaOH) at  $t=0$  and  $t=2\text{h}$  have been considered. Both **Ru1-GC** (acidic conditions) and **Ru2-GC** (basic conditions) show the lowest  $\eta_{10}(t=0)$  ( $20$  and  $25 \text{ mV}$ , respectively) among the reported systems (see Tables S5 and S6). Thus, **Ru1-GC** and **Ru2-GC** outperform Pt in both electrolytes, which shows  $\eta_{10}$  of  $50$  (**Ru1-GC**, 1M  $\text{H}_2\text{SO}_4$ ) and  $30 \text{ mV}$  (**Ru2-GC**, 1 M NaOH) and an increase to  $60 \text{ mV}$  in both media after 2h of electrolysis. The specific current density values observed at  $\eta = 100 \text{ mV}$  ( $0.55 \text{ mA}\cdot\text{cm}^{-2}$  for **Ru1-GC** in acidic media and  $0.19 \text{ mA}\cdot\text{cm}^{-2}$  for **Ru2-GC** in basic media) are between 7 and 137 times higher than those reported for all the benchmarked catalysts except Pt which, despite of the same order, shows superior values (see Tables S5 and S6).

Further information about the intrinsic electrocatalytic activity of our Ru nanomaterial was obtained by calculating TOF values. This was made on the basis of estimated numbers of active sites determined through the underpotential deposition (UDP) of copper onto Pt/C, Rub and **Ru1-GC** in acidic solution (Figure S16). The calculated TOF values for **Ru1-GC** in 1 M  $\text{H}_2\text{SO}_4$  at  $25$ ,  $50$  and  $100 \text{ mV}$  (vs. RHE) are  $0.55$ ,  $3.06$  and  $17.38 \text{ s}^{-1}$ , respectively, which are of the same order than those of Pt/C ( $1.65$ ,  $5.60$  and  $23.36 \text{ s}^{-1}$ ) under the same reaction conditions (Table S1 and Figure S17). Tables S1-S2 allow to compare these TOF values with those reported for other relevant electrocatalysts for a wide set of transition metals, which highlights the fast kinetics of **Ru1-GC**, which outperforms the other systems.

Together with kinetic data, long-term stability is a key parameter for a catalyst to be potentially useful in the HER. Thus, both **Ru1-GC** (1 M  $\text{H}_2\text{SO}_4$ ) and **Ru2-GC** (1 M NaOH) electrodes were held at a constant current density of  $j = -10 \text{ mA}\cdot\text{cm}^{-2}$  in a current-controlled experiment for 12h monitoring the change on the required overpotential.

As shown in Figure 3c, **Ru1-GC** showed negligible change in the required overpotential and identical LSV polarization curves before and after catalytic turnover. In basic media, **Ru2-GC** also shows good stability, with  $\eta_{10}$  increasing in only 25 mV over the 12h electrolysis (Figure 3d). The notorious long-term stability of **Ru2-GC** in basic media is further evidenced by comparison with that of Pt/C under the same conditions (Figure S18), where  $\eta_{10}$  increases in more than 250 mV over the 12h electrolytic test. The excellent durability of our catalytic system in acidic and basic conditions indicates both, good mechanical stability of the cathode (no need of polymeric gluing agents between RuNPs and GC) and no aggregation of the RuNPs under turnover conditions. We believe these findings link to the presence of the PP capping ligand that allows maintaining the nanostructured character of the material. In fact, after catalytic turnover in both acidic and basic conditions small RuNPs are still visible on TEM images, showing the high stability of our nanocatalysts (Figures S19 and S20, respectively). In addition, a Faradaic efficiency of 95% was determined in both cases thus confirming the production of H<sub>2</sub> as the sole reaction taking place (Figures S21 and S22).<sup>35</sup>

## CONCLUSIONS

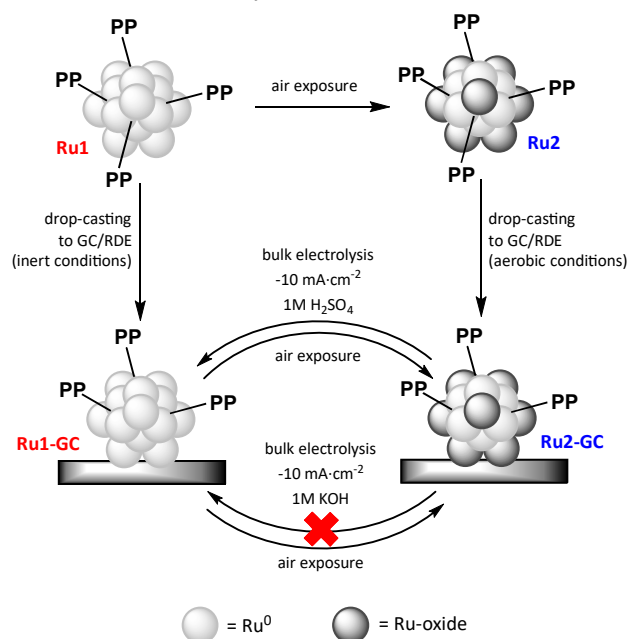
In summary, the application of the organometallic approach as synthetic method allowed obtaining very small and homogeneous-in-size, 4-phenylpyridine-capped RuNPs that are highly active for the HER in both acidic and basic media. DFT-calculations on a 1 nm RuNP with 1.20 H/Ru<sub>surf</sub> composition have shed some light on the coordination of the 4-phenylpyridine ligand at the particle surface in the as-prepared nanomaterial, suggesting the coexisting of both  $\sigma$  and  $\pi$  grafting modes. After controlled partial surface oxidation, the catalytic activity of the resulting GC-deposited nanomaterial (**Ru2-GC**) in 1 M H<sub>2</sub>SO<sub>4</sub> solution is highly dependent on the oxidation state of the NPs' surface, being metallic Ru sites clearly more active than RuO<sub>2</sub> ones. Maximization of the former's from the starting Ru/RuO<sub>2</sub> mixture while preserving the stabilizing ligand (**Ru1-GC**) is achieved through a short reductive treatment in the acidic electrolyte. In contrast, as evidenced by XPS, the original Ru/RuO<sub>2</sub> mixture present in **Ru2-GC** is preserved when 1 M NaOH is used, even under reductive catalytic conditions (Scheme 2).

The estimation of surface active sites and electroactive surface area by well established methods allowed benchmarking these catalytic systems with other relevant catalysts in the literature, confirming them as two of the best HER electrocatalysts reported so far. Thus, in 1 M NaOH solution, **Ru2-GC** displays very low overpotentials ( $\eta_0 \approx 0$  mV,  $\eta_{10} = 25$  mV) and superior to those of commercial Pt/C and Ru, to which also fairly outperform in short and long-term stability tests by well preserving the RuNPs under catalytic turnover. In 1M H<sub>2</sub>SO<sub>4</sub> **Ru1-GC** beats commercial Ru black and is competitive or even superior to commercial Pt/C. It works at very low overpotentials ( $\eta_0 \approx 0$  mV,  $\eta_{10} = 20$  mV), presents a particularly low Tafel slope (29 mV·dec<sup>-1</sup>), achieves TOFs as high as 17 s<sup>-1</sup> at  $\eta = 100$  mV and high specific current densities at  $\eta = 100$  mV of 0.55 mA·cm<sup>-2</sup>, and is capable to produce a current density of 10 mA·cm<sup>-2</sup> for at least 12h without any sign of

deactivation while preserving the morphology of the nanocatalyst.

Although it is not easy to evaluate the exact role played by surface species in the good performance of these RuNPs regarding HER, DFT calculations can provide some clues. A relevant analysis is often done using the *d*-band center model, which underlying principle is that the binding energy of an adsorbate to a metal surface is largely dependent on the electronic structure of the surface itself and it is related to the center of mass of the *d*-band of surface metal atoms with respect to the Fermi energy (*i.e.* the surface *d*-band center,  $\epsilon_{d,surf}$ ).<sup>36,37</sup> When comparing *d*-band center and atomic charge values (Figure S23) it can be noticed that whereas the 53 hydrides significantly stabilize the *d*-band of surface metal atoms with respect to the Fermi energy ( $\epsilon_{d,surf}$ : -2.58 eV in Ru<sub>55</sub> vs. -2.87 in Ru<sub>55</sub>H<sub>53</sub>), the 11 PP ligands have a moderate effect on  $\epsilon_{d,surf}$  (-2.94 eV in Ru<sub>55</sub>H<sub>53</sub>PP<sub>11</sub>). In other words, the PP capping ligands do not significantly alter the surface electronic structures of the metal nanocatalyst (Figure S23). Given DFT adsorption energies, the contribution of PP ligands in the HER process could stem from their rather moderate adsorption strength which allows a large number of hydrogen atoms to be present on the Ru surface. This behavior is different from that for example of strongly coordinated ligands such as CO which impede the presence of surface H atoms in a large range of experimental conditions.<sup>28</sup>

All together, these results highlight the potential of designing and preparing ligand-stabilized nanoparticles as catalysts for the HER and, therefore, paves the way to the fine tuning of the catalytic properties of these nanocatalysts through the limitless strategy of ligand capping, as done for molecular catalysts.



**Scheme 2.** Preparation strategy for the RuNPs systems and electrodes used in this work. Grey spheres mean Ru metal atoms, while darker spheres mean Ru oxide.

## MATERIALS AND METHODS

**Reagents.** All operations for the synthesis of the phenylpyridine-capped Ru nanoparticles were carried out using standard Schlenk tubes, Fisher–Porter bottle techniques or in a glove-box (MBraun) under argon atmosphere. Solvents (THF and pentane) were purified before use, by filtration on adequate column in a purification apparatus (MBraun) and handled under argon atmosphere. Solvents were degassed before use according to a freeze–pump–thaw process. The ruthenium precursor, [Ru(cod)(cot)], was purchased from Nanomeps-Toulouse. Hydrogen gas (Alphagaz) was purchased from Air Liquide. 4-Phenylpyridine (PP) used as a stabilizer was purchased from Sigma-Aldrich and used as received. High purity deionized water was obtained by passing distilled water through a nanopore Milli-Q water purification system.

**Synthesis of RuNPs.** (120 mg, 0.38 mmol) of [Ru(cod)(cot)] and (12 mg, 0.08 mmol) of 4-phenylpyridine were dissolved under argon in 120 mL of THF in a Fisher porter reactor inside a Glove-box. After pressurization of the reactor with 3 bar of H<sub>2</sub> at room temperature (r.t.), the initial yellow solution turned dark brown in a few minutes. A vigorous magnetic stirring and the H<sub>2</sub> pressure were maintained for 16 h. After this reaction time, the H<sub>2</sub> pressure was evacuated and a drop of the colloidal solution was deposited onto a carbon-covered copper grid for TEM analysis. The Ru nanomaterial was isolated as a black powder after precipitation by pentane addition and evaporation to dryness under vacuum.

**Characterization.** The crude colloidal solution has been characterized by Transmission Electron microscopy (TEM), High resolution electron microscopy (HRTEM) and the isolated solid by Wide-angle X-Ray scattering (WAXS), X-Ray photoelectron spectroscopy (XPS), Elemental analysis (EA) and ThermoGravimetric Analysis (TGA).

**Transmission Electron Microscopy (TEM) and High resolution TEM (HRTEM)** were performed at the “Centre de Microcaractérisation Raymond Castaing” in Toulouse (UMS-CNRS 3623). Samples for transmission electron microscopy (TEM) analyses were prepared by slow evaporation of a drop of the crude colloidal solution deposited onto a carbon-covered copper grid. Samples for high-resolution transmission electron microscopy (HRTEM) analyses were prepared by the same way from purified NPs redispersed in THF. TEM and HRTEM analyses were performed on a MET JEOL JEM 1011 microscope operating at 100 kV with a point resolution of 0.45 nm and a JEOL JEM-ARM 200F microscope working at 200 kV with a point resolution lower of 0.19 nm, respectively. TEM allowed to evaluate the particle size, size distribution and morphology. Enlarged micrographs were used for treatment with ImageJ software to obtain a statistical size distribution and the nanoparticle mean diameter. FFT treatments of HRTEM images were carried out with Digital Micrograph Version 1.80.70 to determine the crystalline structure of the material.

**Wide-angle X-Ray scattering (WAXS).** Measurements were performed at CEMES-CNRS in Toulouse. Samples were sealed in 1.0 mm diameter Lindemann

glass capillaries. The samples were irradiated with graphite monochromatized molybdenum K $\alpha$  (0.071069 nm) radiation and the X-ray scattering intensity measurements were performed using a dedicated two-axis diffractometer. Radial distribution functions (RDF) were obtained after Fourier transformation of the corrected and reduced data.

**X-Ray Photoelectron Spectra (XPS).** Measurements were performed at the Catalan Institute of Nanoscience and Nanotechnology (ICN2) in Barcelona with a Phoibos 150 analyzer (SPECS GmbH, Berlin, Germany) in ultra-high vacuum conditions (base pressure 5E-10 mbar) with a monochromatic aluminium K $\alpha$  x-ray source (1486.74 eV). The energy resolution was measured by the FWHM of the Ag 3d<sup>5/2</sup> peak for a sputtered silver foil was 0.62 eV.

**ThermoGravimetric Analysis (TGA).** Thermo-gravimetric analysis was performed in a Perkin Elmer TGA 7 analyzer. Measurements were carried out in a 30–500 °C temperature range in continuous heating regimes (2 °C/min) under Ar atmosphere. The percentage of ligand in the sample was calculated as follows. From the experiment carried out on the ligand alone we could attribute the beginning of the ligand loss at 140 °C. So, the value of loss noticed at this temperature was taken as initial value. For the final ligand loss point, the value observed at the change of the slope was taken. The latter was then subtracted from the former to obtain the ligand percentage on each sample.

**Elemental analysis (EA).** EA was performed at the Laboratoire de Chimie de Coordination (LCC), Toulouse, on a Perkin-Elmer 2400 series II analyzer.

**PP/Ru calculation.** Number of mol ( $n$ ) of PP was calculated from N wt.% obtained by EA and estimated Ru wt.%Ru wt.% was estimated from a) remaining wt.% after TGA's drop in the 130–250 °C range, attributed to organics and b) remaining wt.% subtracting organics (CHN) from EA results. Then, dividing  $n(\text{PP})$  by  $n(\text{Ru})$  gave rise to comparable ligand-to-metal ratios through calculations from both TGA/EA data.

**Electrochemical measurements.** All the electrochemical experiments were performed in a BioLogic SP-150 potentiostat. Rotating disk electrode (RDE) was rotated at 3000 rpm in order to ensure complete removal of *in-situ* formed H<sub>2</sub> bubbles. The solutions were degassed previous to the electrochemical analysis with a N<sub>2</sub> flow. Ohmic potential (IR) drop was automatically corrected at 85 % using the Biologic EC-Lab software for cyclic voltammetry and chronoamperometry. For chronopotentiometry experiments IR drop was manually corrected at 85% by adding the corresponding potential value  $E_{\text{IR}} = i_{\text{exp}} \times (R_{\text{mes}} \times 0.85)$ , where  $i_{\text{exp}}$  is the applied current in A and  $R_{\text{mes}}$  is the measured resistance in  $\Omega$ . 1 M H<sub>2</sub>SO<sub>4</sub> solution was prepared by mixing 56.1 mL of 95–97 % H<sub>2</sub>SO<sub>4</sub> in 1 liter of Mili-Q water. 1 M NaOH solution was prepared by mixing 4 g in 100 mL of Mili-Q water.

A rotating disk electrode (RDE,  $\phi = 0.3$  cm,  $S = 0.07$  cm<sup>2</sup>) was used as working electrodes (WE), except for the hydrogen-monitored bulk electrolysis that a Fluorine-doped Tin Oxide electrode (FTO, 20 mm x 10 mm x 180  $\mu\text{m}$ ) was used. In the case of FTO the surface dipped in the



electrochemical solution was 1 cm<sup>2</sup>. For FTO electrode the experiment was magnetically stirred with a stirring bar. A Pt grid was used as counter electrode (CE) and a Saturated Calomel Electrode (SCE, KCl sat.) electrode was used as a reference electrode (RE), except for the hydrogen-monitored bulk electrolysis that a Ag/AgCl (KCl sat.) was used as RE. All data was transformed to RHE by adding +0.24 V and 0.20 V for SCE and Ag/AgCl RE respectively.

**Electrode Preparation.** A 2 mg·mL<sup>-1</sup> dispersion was prepared by adding 1 mg of RuX (X=1, 2) in 500 μL of THF and sonicating for 30 min. Then, an aliquot of 5 μL (for GC<sub>d</sub> and RDE) was added on the surface of the GC (*S* = 0.07 cm<sup>2</sup>), and dried with a N<sub>2</sub> flow. This procedure was repeated three times to obtain RuX-GC (X=1, 2). For FTO WE, a dispersion aliquot of 25 μL was added to the surface of the FTO (*S* = 1 cm<sup>2</sup>), and dried with a N<sub>2</sub>. See Scheme S1 for schematic representation. For Pt/C and Rub, dispersions ensuring a similar metal mass loading on the RDE than for RuX-GC were prepared.

**Double-layer capacitance (*C<sub>DL</sub>*) and electrochemical active surface area (ECSA) determination.** *C<sub>DL</sub>* was estimated by CV. A non-Faradaic region was chosen from the LSV (typically a 0.1 V window about OCP), where no redox process takes place and all the measured current is due to double-layer charging (versus SCE, 0.35 V for 1 M H<sub>2</sub>SO<sub>4</sub> and -0.35 V for 1 M NaOH). Based on this assumption, the charging current (*i<sub>c</sub>*) can be calculated as the product of the electrochemical double-layer capacitance (*C<sub>DL</sub>*) and the scan rate (*v*), as shown in Eq. 1:

$$i_c = vC_{DL} \quad \text{Eq. 1}$$

Plotting *i<sub>c</sub>* as a function of *v* yields a straight line with slope equal to *C<sub>DL</sub>*. In this way, 8 different scan rates were used (5, 10, 25, 50, 75, 100, 250 and 500 mV/s), holding the working electrode at each potential vertex for 10 seconds prior to the next step.

ECSA was obtained by dividing the calculated capacitance to a tabulated value (specific capacitance, *C<sub>S</sub>*) that depends on the material used and solution (for C, in 1M H<sub>2</sub>SO<sub>4</sub> *C<sub>S</sub>*=13-17 μF·cm<sup>-2</sup>, in 1 M NaOH *C<sub>S</sub>*= 40 μF·cm<sup>-2</sup>):

$$ECSA[cm^2] = \frac{C_{DL}}{C_S} \quad \text{Eq. 2}$$

$$RF = \frac{ECSA}{S} \quad \text{Eq. 3}$$

Roughness factor (RF) was calculated by dividing the ECSA by the geometrical surface area (*S*).

**TOF (s<sup>-1</sup>) calculations.** TOF where calculated as follows:

$$TOF(s^{-1}) = \frac{I}{2Fn} = \frac{I}{Q_{Cu}} \quad \text{Eq. 4}$$

where *I* is the current intensity on the LSV measurement, *F* is the Faradaic constant, and *n* the number of active sites obtained by the UPD method.

*Q<sub>Cu</sub>* and *n* were calculated from copper under potential deposition method (UPD). In a 20 mL cell containing a Pt grid as CE and a SCE as RE, a 1 M H<sub>2</sub>SO<sub>4</sub> pH = 0 was prepared with 5 mM CuSO<sub>4</sub> concentration, and a bulk electrolysis at 0.24 V was applied for 100s. A LSV was performed before and after the bulk electrolysis in a clean pH=0 solution without any presence of Cu (*E<sub>i</sub>* = 0.04 V, *E<sub>f</sub>*

= 0.89 V, 10 mV/s), and a new wave devoted to the oxidation of deposited Cu appeared at *E* = 0.41 V.

The area under the oxidative wave, or Cu-UPD stripping charge (*Q<sub>Cu</sub>*, *Q<sub>UPD</sub>*), was determined and used for the calculation of the number of active sites (*n*):

$$Cu_{UPD} \rightarrow Cu^{2+} + 2\bar{e} \quad \text{Eq. 5}$$

$$n[mol] = \frac{Q_{Cu}}{2F} \quad \text{Eq. 6}$$

, where *F* is the Faraday constant (96485 C·mol<sup>-1</sup>).

**DFT calculations.** The Ru<sub>55</sub> model has previously been published and detailed elsewhere.<sup>28</sup> Briefly, it was shaped by slicing an hcp structure by two (001) and (101) planes. A tip has been added in order to introduce one B<sub>4</sub> and one B<sub>5</sub> site. Removing one line of atoms between two (101) planes generates a slightly corrugated facet. Such defects can probably be found on NPs larger than this ultra-small 1nm model. It is now well known that bare Ru surfaces cannot explain the actual adsorption properties on hydrogenated surfaces. The surface was then covered with 1.2 hydrides per surface ruthenium atom, a usually measured coverage value on RuNPs.<sup>27</sup> In this resulting Ru<sub>55</sub>H<sub>53</sub> model, the dissociative adsorption energy per hydrogen atom (*E<sub>ads</sub>* = [E(Ru<sub>55</sub>H<sub>53</sub>) - E(Ru<sub>55</sub>) - (53/2)E(H<sub>2</sub>)]/53) is found to be -13.2 kcal·mol<sup>-1</sup> at the DFT level of approximation used in this study. DFT calculations were done with the Vienna ab initio simulation package, VASP,<sup>38,39</sup> spin polarized DFT; exchange-correlation potential approximated by the generalized gradient approach proposed by Perdew, Burke, and Ernzerhof (PBE);<sup>40</sup> projector augmented waves (PAW) full-potential reconstruction;<sup>41,42</sup> PAW data sets for Ru atoms treating the 4*p*, 4*d* and 5*s* states (14 valence electrons); kinetic energy cutoff: 500 eV;<sup>27</sup> Γ-centered calculations;<sup>43</sup> Gaussian smearing of 0.02 eV width; geometry optimization threshold: residual forces on any direction less than 0.02 eV/Å; supercell size set to ensure a vacuum space of ca. 12 Å between periodic images of metal clusters, *i.e.* 30.5Å x 30.5Å x 31Å for Ru<sub>55</sub>H<sub>53</sub>PP<sub>12</sub>). The d-band center<sup>36</sup> values were calculated after projection by the Lobster software<sup>44</sup> of the planewave/pseudopotential wavefunction on a local Slater atomic basis set.

## ASSOCIATED CONTENT

**Supporting Information.** TEM, EDX, WAXS, H<sub>2</sub> measurements, EA, DFT and electrochemical data are depicted in the Supporting Information. This material is available free of charge via the Internet at <http://pubs.acs.org>.

## AUTHOR INFORMATION

### Corresponding Author

\* E-mail : Xavier Sala, [xavier.sala@uab.cat](mailto:xavier.sala@uab.cat)  
 \* E-mail : Jordi Garcia-Anton, [Jordi.GarciaAnton@uab.es](mailto:Jordi.GarciaAnton@uab.es)  
 \* E-mail : Karine Philippot, [karine.philippot@lcc-toulouse.fr](mailto:karine.philippot@lcc-toulouse.fr)

### ORCID numbers

Jordi Creus: 0000-0001-5555-8122  
 Samuel Drouet: 0000-0003-1814-7556

Pierre Lecante: 0000-0001-6337-6855  
Romuald Poteau: 0000-0003-4338-174X  
Karine Philippot: 0000-0002-8965-825X  
Jordi García-Antón: 0000-0002-2401-0401  
Xavier Sala: 0000-0002-7779-6313

#### Notes

The authors declare no competing financial interest

#### ACKNOWLEDGMENT

This work was financially supported by the MINECO/FEDER project CTQ2015-64261-R, the CNRS, the University Paul Sabatier – Toulouse, the IDEX UNITI Emergence project (UFTMIP: 2015-209-CIF-D-DRD-127185), the CTP regional action (Catalunya/n° CTP2013-0016 and Midi-Pyrénées/n°13053026) and the GDRI HC3A franco-catalan action. J.C. thanks UAB and “Euroregió Pirineus Mediterrànea” for PhD grants. J.G.-A. acknowledges Serra Hünter Program. R.P. thanks the HPCs CALcul en Midi-Pyrénées (CALMIP-EOS, grant P0611) and the Grand Equipement National de Calcul Intensif (GENCI-TGCC, grant o810168) for generous allocations of computer time. The authors acknowledge Guillaume Sauthier for XPS analysis.

#### REFERENCES

- Berardi, S.; Drouet, S.; Francàs, L.; Gimbert-Suriñach, C.; Guttentag, M.; Richmond, C.; Stoll, T.; Lobet, A. Molecular Artificial Photosynthesis. *Chem. Soc. Rev.* **2014**, *43*, 7501-7519.
- Coutard, N.; Kaeffer, N.; Artero, V. Molecular Engineered Nanomaterials for Catalytic Hydrogen Evolution and oxidation. *Chem. Commun.* **2016**, *52*, 13728-13748.
- Eftekhari, A. Electrocatalysts for Hydrogen Evolution Reaction. *Int. J. Hydrogen Energy* **2017**, *42*, 11053-11077.
- Philippot, K. and Serp, P. in *Nanomaterials in Catalysis*, P. Serp, P and Philippot, K. (Eds.), Wiley-VCH, Weinheim, 2013, Chapter 1, 1-54.
- Weiping, X.; Lei, W.; Gong, M.; Xin, H. L.; Wang, D. Recent Advances of Structurally Ordered Intermetallic Nanoparticles for Electrocatalysis. *ACS Catal.* **2018**, *8*, 3237-3256.
- Astruc D. (Ed.), *Nanoparticles and Catalysis*, Wiley-VCH, Weinheim, 2008.
- Schmid G. (Ed.), *Clusters and Colloids. From Theory to Applications*, Wiley- VCH, Weinheim, 1994.
- Bhowmik, T.; Kundu, M. K.; Barman, S. Growth of One-Dimensional RuO<sub>2</sub> Nanowires on g-Carbon Nitride: An Active and Stable Bifunctional Electrocatalyst for Hydrogen and Oxygen Evolution Reactions at All pH Values. *ACS Appl. Mater. Interfaces* **2016**, *8*, 28678-28688.
- Fukuzumi, S.; Yamada, Y. Catalytic Activity of Metal-Based Nanoparticles for Photocatalytic Water Oxidation and Reduction. *J. Mater. Chem.* **2012**, *22*, 24284-24296.
- Li, X.; Hao, X.; Abudula, A.; Guan, G. Nanostructured Catalysts for Electrochemical Water Splitting: Current State and Prospects. *J. Mater. Chem. A* **2016**, *4*, 11973-12000.
- Zeng, M.; Li, Y. Recent Advances in Heterogeneous Electrocatalysts for the Hydrogen Evolution Reaction. *J. Mater. Chem. A*, **2015**, *3*, 14942-14962.
- Kuang, M.; Zheng, G. Nanostructured Bifunctional Redox Electrocatalysts. *Small* **2016**, *12*, 5656-5675.
- Chen, Z.; Lu, J.; Ai, Y.; Ji, Y.; Adschiri, T.; Wan, L. Ruthenium/Graphene-like Layered Carbon Composite as an Efficient Hydrogen Evolution Reaction Electrocatalyst. *ACS Appl. Mater. Interfaces* **2016**, *8*, 35132-35137.
- Demir, E.; Akbayrak, S.; Önal, A. M.; Özkar, S. Nanoceria-Supported Ruthenium(0) Nanoparticles: Highly Active and Stable Catalysts for Hydrogen Evolution from Water. *ACS Appl. Mater. Interfaces* **2018**, *10*, 6299-6308.
- Ye, R.; Liu, Y.; Peng, Z.; Wang, T.; Jalilov, A. S.; Yakobson, B. I.; Wei, S. H.; Tour J. M. High Performance Electrocatalytic Reaction of Hydrogen and Oxygen on Ruthenium Nanoclusters. *ACS Appl. Mater. Interfaces* **2017**, *9*, 3785-3791.
- Zheng, Y.; Jiao, Y.; Zhu, Y.; H.; Li, L.; Han, Y.; Chen, Y.; Jaroniec, M.; Qiao, S. High Electrocatalytic Hydrogen Evolution Activity of an Anomalous Ruthenium Catalyst. *J. Am. Chem. Soc.* **2016**, *138*, 16174-16181.
- Mahmood, J.; Li, F.; Jung, S.; Okyay, M. S.; Ahmad, I.; Kim, S.; Park, N.; Jeong, H. Y.; Baek, J. An Efficient and pH-Universal Ruthenium-Based Catalyst for the Hydrogen Evolution Reaction. *Nature Nanotech.* **2017**, *12*, 441-446.
- Chi, J. Q.; Gao, W. K.; Lin, J. H.; Dong, B.; Yan, K. L.; Qin, J. F.; Liu, B.; Chai, Y. M.; Liu C. G. Hydrogen Evolution Activity of Ruthenium Phosphides Encapsulated in Nitrogen- and Phosphorous-Codoped Hollow Carbon Nanospheres. *ChemSusChem* **2018**, *11*, 743-752.
- Drouet, S.; Creus, J.; Collière, V.; Amiens, C.; Garcia-Antón, J.; Sala, X.; Philippot, K. A Porous Ru Nanomaterial as an Efficient Electrocatalyst for the Hydrogen Evolution Reaction under Acidic and Neutral Conditions. *Chem. Commun.* **2017**, *53*, 11713-11716.
- Wang, Z. L.; Sun, K.; Henzie, J.; Hao, X.; Li, C.; Takei, T.; Kang, Y. M.; Yamauchi, Y. Spatially Confined Assembly of Monodisperse Ruthenium Nanoclusters in a Hierarchically Ordered Carbon Electrode for Efficient Hydrogen Evolution. *Angew. Chem. Int. Ed.* **2018**, *57*, 5848-5852.
- Amiens, C.; Chaudret, B.; Ciuculescu-Pradines, D.; Collière, V.; Fajerweg, K.; Fau, P.; Kahn, M.; Maisonnat, A.; Philippot, K. Organometallic Approach for the Synthesis of Nanostructures. *New J. Chem.*, **2013**, *37*, 3374-3401.
- Amiens, C.; Ciuculescu-Pradines, D.; Philippot, K. Controlled Metal Nanostructures: Fertile Ground for Coordination Chemists. *Coord. Chem. Rev.* **2016**, *308*, 409-432.
- Philippot, K.; Lignier, P.; Chaudret, B. in *Ruthenium in Catalysis 2014*, Bruneau C. and Dixneuf P.H. (Eds), Wiley VCH, Weinheim, 2014, *Top. Organomet. Chem.* **2014**, *48*, 319-370.
- Favier, I.; Massou, S.; Teuma, E.; Philippot, K.; Chaudret, B.; Gómez, M. A New and Specific Mode of Stabilization of Metallic Nanoparticles. *Chem. Commun.* **2008**, *28*, 3296-3298.
- Favier, I.; Lavedan, P.; Massou, S.; Teuma, E.; Philippot, K.; Chaudret, B.; Gómez, M. Hydrogenation Processes at the Surface of Ruthenium Nanoparticles: A NMR Study. *Top Catal.* **2013**, *56*, 1253-1261.
- Ayvali, T.; Philippot, K. in *New Materials for Catalytic Applications*, Kemnitz, E. and Parvulescu, V. (Eds.), Elsevier, 2016, Chapter 3, 41-79.
- García-Antón, J.; Axet, M. R.; Jansat, S.; Philippot, K.; Chaudret, B.; Pery, T.; Buntkowsky, G.; Limbach, H. H. Reactions of Olefins with Ruthenium Hydride Nanoparticles: NMR Characterization, Hydride Titration, and Room-Temperature C–C Bond Activation. *Angew. Chem. Int. Ed.* **2008**, *47*, 2074-2078.
- Cusinato, L.; Martinez-Prieto, L. M.; Chaudret, B.; del Rosal, I.; Poteau, R. Theoretical Characterization of the Surface Composition of Ruthenium Nanoparticles in Equilibrium with Syngas. *Nanoscale*, **2016**, *8*, 10974-10992.

- (29) Johnson, B. F. G.; Lewis, J.; Housecroft, C.; Gallup, M.; Martinelli, M.; Braga, D.; Grepioni, F. The Coordination of Benzene in Clusters: The Face-Capping Mode. *J. Mol. Catal.*, **1992**, *74*, 61-72.
- (30) Walter, M. G.; Warren, E. L.; McKone, J. R.; Boettcher, S. W.; Mi, Q.; Santori, E. A.; Lewis, N. S. Solar Water Splitting Cells. *Chem. Rev.*, **2010**, *110*, 6446-6473.
- (31) Gorlin, Y.; Jaramillo, T. F. A Bifunctional Nonprecious Metal Catalyst for Oxygen Reduction and Water Oxidation. *J. Am. Chem. Soc.*, **2010**, *132*, 13612-13614.
- (32) Morgan, D. M. Resolving ruthenium: XPS studies of common ruthenium materials. *Surf. Interf. Anal.* **2015**, *47*, 1072-1079.
- (33) Shinagawa, T.; Garcia-Esparza, A. T.; Takahabe, K. Insight on Tafel Slopes from a Microkinetic Analysis of Aqueous Electrocatalysis for Energy Conversion. *Sci. Rep.*, **2015**, *5*, 13801-13821.
- (34) McCrory, C. C.; Jung, S.; Ferrer, I. M.; Chatman, S. M.; Peters, J. C.; Jaramillo, T. F. Benchmarking Hydrogen Evolving Reaction and Oxygen Evolving Reaction Electrocatalysts for Solar Water Splitting Devices. *J. Am. Chem. Soc.*, **2015**, *137*, 4347-4357.
- (35) Faradaic efficiencies were quantified by using an H<sub>2</sub> probe and dividing the total amount of H<sub>2</sub> produced by the theoretical one calculated from the total charge passed.
- (36) Hammer, B.; Nørskov, J. K. N. Electronic Factors Determining the Reactivity of Metal Surfaces. *Surf. Sci.* **1995**, *343*, 211-220.
- (37) del Rosal, I.; Mercy, M.; Gerber, I. C.; Poteau, R. Ligand-Field Theory-Based Analysis of the Adsorption Properties of Ruthenium Nanoparticles. *ACS Nano* **2013**, *7*, 9823-9835
- (38) Kresse, G.; Fürthmüller, J. Efficient Iterative Schemes for Ab Initio Total-Energy Calculations Using a Plane-Wave Basis Set. *Phys. Rev. B* **1996**, *54*, 11169-11186.
- (39) Kresse, G.; Fürthmüller, J. Efficiency of Ab Initio Total Energy Calculations for Metals and Semiconductors Using a Plane-Wave Basis Set. *Comput. Mater. Sci.*, **1996**, *6*, 15-50.
- (40) Perdew, J. P.; Burke, K.; Ernzerhof, M. Generalized Gradient Approximation Made Simple. *Phys. Rev. Lett.* **1996**, *77*, 3865-3868.
- (41) Blöchl, P. E. Projector Augmented-Wave Method. *Phys. Rev. B* **1994**, *50*, 17953-17979.
- (42) Kresse, G.; Joubert, D. From Ultrasoft Pseudopotentials to the Projector Augmented-Wave Method. *Phys. Rev. B* **1999**, *59*, 1758-1775.
- (43) Monkhorst, J. D.; Pack, H. J. Special Points for Brillouin-Zone Integrations. *Phys. Rev. B* **1976**, *13*, 5188-5192.
- (44) Maintz, S.; Deringer, V. L.; Tchougréeff; Dronskowski, R. LOBSTER: A Tool to Extract Chemical Bonding from Plane-Wave Based DFT. *J. Comp. Chem.* **2016**, *37*, 1030-1035.

## Table of Contents (TOC)

